Available online at www.sciencedirect.com
ScienceDirect
Trans. Nonferrous Met. Soc. China 32(2022) 2150−2163
Transactions of Nonferrous Metals Society of China
www.tnmsc.cn

Processing map and hot deformation behavior of squeeze cast 6082 aluminum alloy

Lei DENG[1], Hai-dong ZHANG[1], Guo-ai LI[2], Xue-feng TANG[1], Pu-song YI[1], Zhao LIU[1], Xin-yun WANG[1], Jun-song JIN[1]

1. State Key Laboratory of Materials Processing and Die & Mould Technology, Huazhong University of Science and Technology, Wuhan 430074, China;
2. AECC Beijing Institute of Aeronautical Materials, Beijing 100095, China

Received 19 July 2021; accepted 23 February 2022

Abstract: The hot deformation behavior and microstructure evolution of 6082 aluminum alloy fabricated through squeeze casting (SC) under different pressures were studied. The alloy was subjected to hot compression tests and 3D hot processing maps were established. The microstructure evolution was studied by optical microscope (OM), scanning electron microscope (SEM), and electron backscattered diffraction (EBSD). It is found that more dynamic recrystallization (DRX) grains are generated during the deformation of the specimen fabricated under higher SC pressure. At high temperature the effect of SC pressure on microstructure evolution weakens due to the dissolution of second phase particles. In addition, uneven second phase particles in specimens fabricated under higher SC pressure compressed with low temperature and middle strain rate would result in flow localization instability. Finally, the optimum deformation conditions for the 6082 aluminum alloy fabricated by SC were obtained at the temperatures of 430−500 °C and the strain rates of 0.01−1 s^{-1}.

Key words: 6082 aluminum alloy; squeeze casting; deformation behavior; processing map; dynamic recrystallization

1 Introduction

As a typical 6000 series aluminum alloy, 6082 aluminum alloy is widely used in structural parts in the aeronautical and automobile industries due to the high specific strength, good machinability, and excellent thermoplastic forming ability [1−3]. The conventional manufacturing process for many aluminum alloy parts, such as steering knuckle arm and flange, is forging followed by heat treatment and machining. The dynamically recrystallized grains generated during the forging process in the peripheral zone of forgings tend to coarsen at the following heat treatment, leading to the decrease of mechanical properties [4,5]. Recently, the hybrid forming process combining casting and forging attracts much attention since this process can avoid local coarse grains and improve production efficiency when it is used in complex shape components [4,6−8]. BIROL and AKDI [9] adopted the cooling slope casting process to produce EN AW 6082 forging stock for suspension components and discovered that cast billets for forging stock can not only avoid coarse grains but also reduce the production costs by 15%−20%. GUO et al [10] used a new technology known as near-net shape casting for forging stock preparation to produce the automobile suspension and studied DRX behavior during forging. However, the effects of casting parameters on the microstructure evolution have seldom been discussed and the optimum processing parameters, which are critical for producing parts with excellent mechanical properties, have not been investigated.

The aluminum alloy parts usually deform at

Corresponding author: Jun-song JIN, Tel: +86-27-87559815, E-mail: jsjin@hust.edu.cn
DOI: 10.1016/S1003-6326(22)65937-5

elevated temperatures due to the poor formability at room temperature, while the microstructure evolution and flow behavior are complex and greatly influenced by the initial microstructure and hot deformation condition [11−13]. The hot processing maps can be employed as a powerful tool to determine the optimum processing parameters based on the data of true stress−strain curves [14−16]. WANG et al [17] established the 3D processing map of hot-rolled 7050 aluminum alloy, and believed that the high power dissipation areas were induced by the occurrence of DRX, while micro defects resulted in the instable areas. SUN et al [18] investigated the hot workability of 6A02 aluminum alloy through the hot processing map and found that deformation conditions at a temperature higher than 490 °C and a low strain rate are not suitable for acquiring uniform fine recrystallization structure. Thus, hot processing map is an effective method to study the workability of SC billet under different SC pressures and forging conditions, and to determine suitable deformation parameters for high-performance parts with excellent microstructure.

From the brief summary above, it can be seen that the hybrid process which combines squeeze casting and forging is an efficient and low-cost metal forming method in manufacturing high-performance parts with great application potential, while the thermoplastic formability of SC aluminum alloy billet is still not clear. Thus, it is of great importance to study the hot deformation behavior of SC aluminum alloy and to optimize processing parameters. In this study, the 6082 aluminum alloy fabricated by SC under different pressures was subjected to hot compression tests. The microstructure was observed through OM, SEM, and EBSD. Then, the flow behavior was analyzed and the processing maps under different SC pressures were established. The effects of SC pressures and compression conditions on microstructure evolution were discussed in detail and the optimum deformation condition was obtained.

2 Experimental

6082 aluminum alloy was used in this study. The raw material was melted at 750 °C in a furnace. After degassing, holding, and deslagging, SC experiments were performed on a vertical SC machine. The pouring temperature was set to be 730 °C, the SC pressures were 50 and 100 MPa, and the holding time was 90 s. Then, the SC 6082 aluminum alloy bars were obtained. As shown in Table 1, the chemical composition was measured by an optical emission spectrometer (PDA7000).

Table 1 Chemical composition of 6082 aluminum alloy (wt.%)

Element	Standard	Measured
Si	0.7–1.3	0.83
Mg	0.6–1.2	0.819
Mn	0.4–1.0	0.539
Cr	0.25	0.126
Zn	≤0.2	0.113
Cu	≤0.1	0.097
Fe	≤0.5	0.023
Al	Bal.	Bal.

The hot compression specimens with sizes of 8 mm in diameter and 12 mm in height were sectioned from the bars fabricated under the SC pressures of 50 and 100 MPa (hereafter referred to as S50 and S100, respectively for convenience). The hot compression tests were performed on a Gleeble−3500 thermal simulator by the following experimental procedure illustrated in Fig. 1. The specimens were heated to 530 °C with a heating rate of 2 °C/s and held for 3 min to homogenize the composition in the α(Al) matrix, and the influence of the preheating treatment on the second phase particle distribution and the grain size can be ignored for the short holding time. Then, the specimens were cooled down to the deformation temperatures with a cooling rate of 5 °C/s and held for 3 min. The compression tests were carried out at a series of different deformation temperatures (350, 400, 450 and 500 °C) and strain rates (0.01, 0.1, 1 and 10 s^{-1}) with a true strain of 0.69. To retain the microstructure after hot deformation, water quenching was conducted immediately after compression.

The initial SC samples were sectioned from the bars and mechanically polished followed by etching with Keller's reagent for about 30 s. The

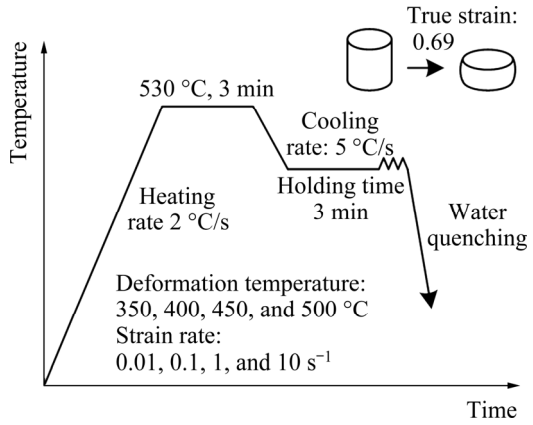

Fig. 1 Procedure of hot compression tests

microstructure of SC samples was observed by an optical microscope (OLYMPUS BX61) and a field emission scanning electron microscope (FESEM, FEI Quanta 650) equipped with an element energy dispersive spectrometer (EDS) system and an electron backscattered diffraction (EBSD) system. The specimens after hot deformation were sliced along the compression axial and mechanically polished, followed by electrolytic polishing with 10 vol.% $HClO_4$ in alcohol at a voltage of 20 V for 12 s. Then, EBSD analysis was carried out on the FESEM and the distribution of the second phase particles was observed using an electron probe micro analyzer (EPMA, EPMA−8050G).

3 Results and discussion

3.1 Microstructure of SC samples

Optical micrographs of 6082 aluminum alloy fabricated by SC under pressures of 100 and 50 MPa are shown in Figs. 2(a) and (b), respectively, and the α(Al) phase in both samples is characterized

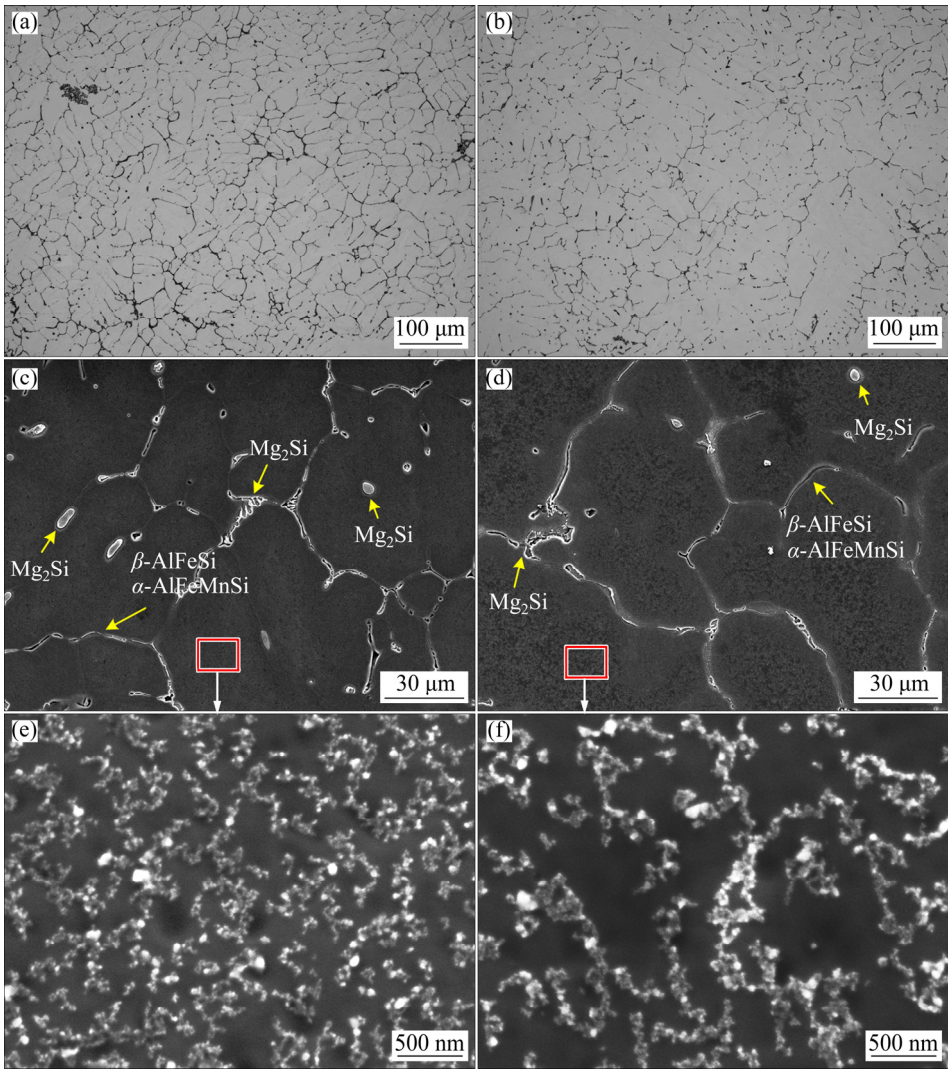

Fig. 2 OM (a, b) and SEM (c, d, e, f) images of SC samples fabricated under different pressures: (a, c, e) 100 MPa; (b, d, f) 50 MPa

by typical dendritic shape. Compared with those of S50, the grain size and secondary dendrite arm spacing (SDAS) of S100 are finer. The SDAS values of S50 and S100 are 18.6 and 16.4 μm, respectively. According to GHOMASHCHI and VIKHROV [19], the effect of SC pressure (p) on freezing point can roughly be estimated as

$$p = p_0 \exp\left(\frac{-\Delta H_f}{RT_f}\right) \quad (1)$$

where ΔH_f is the latent heat of fusion, T_f is the equilibrium freezing temperature, p_0 and R are constants. According to Eq. (1), the equilibrium freezing point T_f will increase with the increasing pressure p, which results in large undercooling and high grain nucleation rate, i.e., there will be more atomic groups involved in crystallization, leading to the refinement of microstructure. Additionally, the alloy and mould contact more intimately because higher pressure could result in the reduction of the air gap, and the transfer coefficient and the nucleation rate become higher, thus finer microstructure is possibly obtained [20].

As can be seen in Figs. 2(c) and (d), the SEM results show that second phase particles are formed between α(Al) dendrites during the cooling stage in the SC process and S100 contains more second phase particles than S50. According to the EDS results, the second phase particles at grain boundaries are the mixture of β-Mg_2Si, β-AlFeSi, and α-AlFeMnSi, while the second phase particles precipitated in the matrix are mostly β-Mg_2Si, which is consistent with Ref. [21]. The volume fraction of second phase particles of S100 (5.63%) is higher than that of S50 (3.06%), but the average equivalent diameter of the two samples is similar (37.9 and 37.4 μm, respectively). Figures 2(e) and (f) show the distribution of dispersoids in the α(Al) matrix marked by red rectangles in Figs. 2(c) and (d), respectively, and a large number of dispersoids are observed in both samples and the dispersoids in S100 are more and finer.

3.2 Hot deformation behavior

Figure 3 presents the true stress−true strain curves of S50 and S100 samples deformed at various

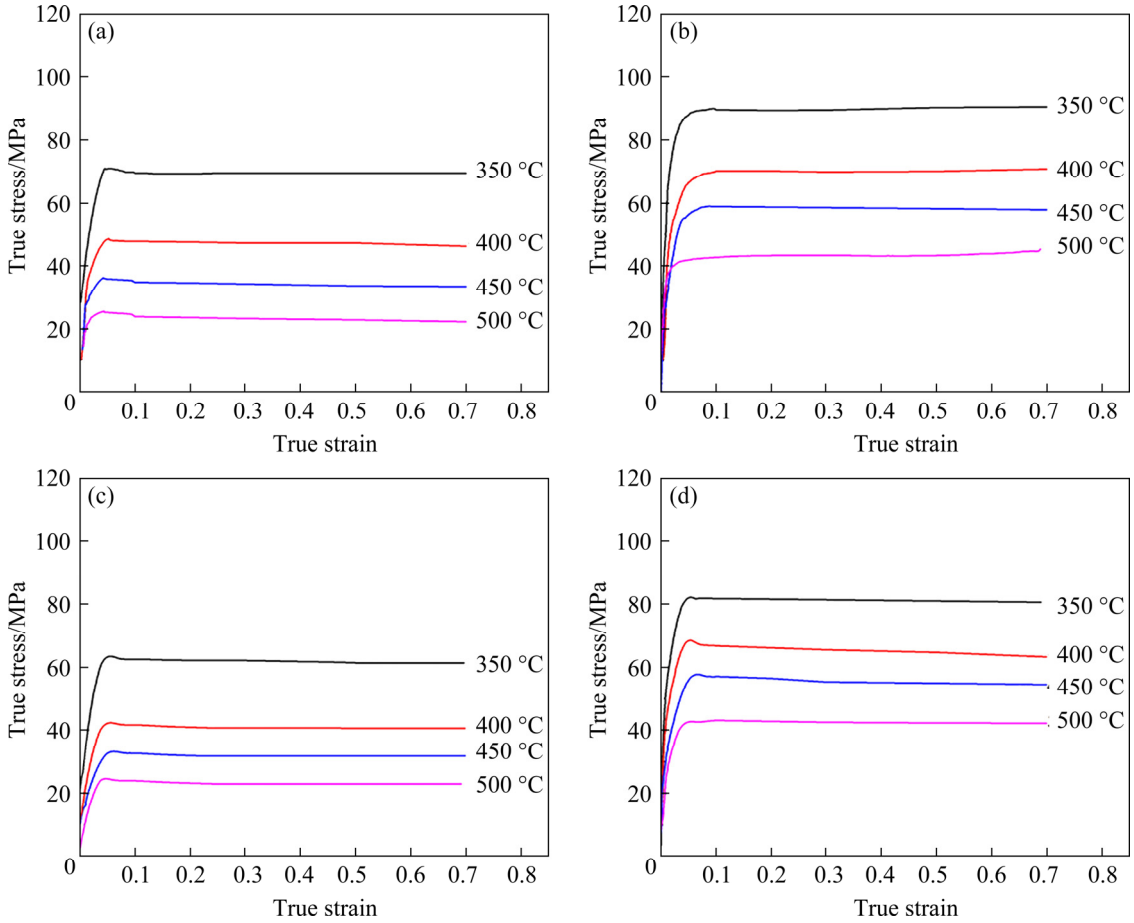

Fig. 3 True stress−true strain curves during hot compression tests of S100 (a, b) and S50 (c, d) at different temperatures and strain rates: (a, c) 0.01 s^{-1}; (b, d) 1 s^{-1}

temperatures and strain rates. As the strain increases, the flow stress increases sharply at the initial stage and then reaches an approximately steady-state with a slight decrease. The flow stress increases with the increase of the strain rate and decreases with the increase of the temperature, which is in agreement with previous research [22−25]. Figure 4 displays the corresponding flow stress at the strain of 0.69. It can be seen that higher SC pressure samples present higher flow stress under the same deformation condition. One reason for such difference could be that the microstructure of S100 is finer than that of S50. The dislocation slip is restricted at small grains and the flow stress is higher. Furthermore, more second phase particles in S100 result in stronger second phase strengthening. According to the precipitation strengthening mechanism $\Delta\sigma_p=cf^{0.5}r^{-1}$ ($\Delta\sigma_p$ is the stress increment due to precipitation strengthening, f is the volume fraction of precipitated phase, r is the radius of the precipitated phase, and c is alloy constant) [26], more and finer dispersoids in S100 result in a higher strengthening effect.

From Fig. 4, the difference between the flow stress of the aluminum alloy under different SC pressures decreases with the increasing temperature. The possible reasons are demonstrated as follows. Firstly, the dislocations are easier to climb or slide at higher temperatures, thus dislocation pile-ups in S50 and S100 are both reduced. Secondly, grain rotation and grain boundary sliding become significant as the temperature increases, thus, S100 presents more stress reduction as finer grain structure contains higher fraction of the grain boundary [27]. Thirdly, regardless of the different contents of the second phase particles in these two kinds of specimens, the pining effects are both weakened to a similarly low level since these particles are dissolved in large quantities at high temperatures. During the compression tests, the specimens fabricated under different SC pressures are in a similar state at high temperatures. As a result, the gap of the flow stresses between S100 and S50 gradually is reduced with the increasing temperature.

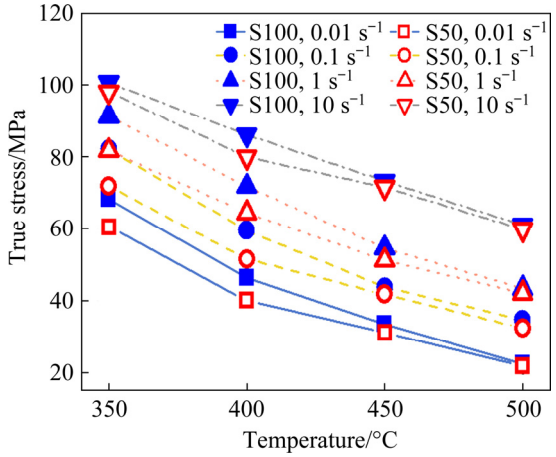

Fig. 4 Flow stress of S100 and S50 at strain of 0.69 under different deformation conditions

3.3 Hot processing map

3.3.1 Framework of hot processing map

The hot processing map has been widely used to analyze the deformation mechanism of materials and optimize process parameters. This method is based on a dynamic material model (DMM) which elaborates on the relationship between heat energy induced by the plastic deformation and energy dissipation consumed by microstructure evolution during deformation. According to DMM, power dissipation during hot deformation consists of two parts, which can be expressed as [28]

$$P=\sigma\dot{\varepsilon}=\int_0^{\dot{\varepsilon}}\sigma\mathrm{d}\dot{\varepsilon}+\int_0^{\sigma}\dot{\varepsilon}\mathrm{d}\sigma=G+J \tag{2}$$

where P is the power dissipation, $\dot{\varepsilon}$ is the strain rate, σ is the stress, G refers to the power dissipation generated from hot deformation, and J represents the power dissipation aroused from microstructure evolution. Based on Eq. (2), the relationship between G and J can be revealed as follows [29]:

$$\sigma=K\dot{\varepsilon}^m \tag{3}$$

$$\left(\frac{\partial J}{\partial G}\right)_{\varepsilon,T}=\frac{\dot{\varepsilon}\mathrm{d}\sigma}{\sigma\mathrm{d}\dot{\varepsilon}}=\left[\frac{\partial(\ln\sigma)}{\partial(\ln\dot{\varepsilon})}\right]_{\varepsilon,T}=m \tag{4}$$

where K is a constant, m stands for the strain rate sensitivity index of the material, and J can be expressed as

$$J=\int_0^{\sigma}\dot{\varepsilon}\mathrm{d}\sigma=\frac{m}{m+1}\sigma\dot{\varepsilon} \tag{5}$$

From Eq. (5), J reaches the maximum value (J_{max}) when m=1, which can be expressed as

$$J_{max}=\frac{\sigma\dot{\varepsilon}}{2} \tag{6}$$

In the hot processing map, the non-dimensional power dissipation efficiency (η) is used to describe the relationship between the power

dissipated by the microstructure evolution and total power during the forming process [29,30]. And η is given as

$$\eta = \frac{J}{J_{\max}} = \frac{2m}{m+1} \tag{7}$$

The instability model is based on the principle of irreversible thermodynamics of large plastic flow. The instability criterion can be represented according to the principle of energy dissipation, which is given by [30,31]

$$\xi(\dot{\varepsilon}) = \frac{\partial \ln\left(\frac{m}{m+1}\right)}{\partial \ln \dot{\varepsilon}} + m < 0 \tag{8}$$

With the values of η and ξ, the hot processing map can be established with the instability map and power dissipation map. Generally, the high power dissipation efficiency can reduce the occurrence of flow instability, promote DRX and contribute to the steady-state flow, and material processing performance will be improved. Compared with the regular hot processing map, the 3D hot processing map integrates strain with strain rate and temperature, which has higher accuracy in describing the processing condition [17].

3.3.2 Analysis of hot processing map

As shown in Fig. 5, the 3D power dissipation maps and the 3D instability maps of S100 and S50 were established. It can be seen from Fig. 5(a) and Fig. 5(c) that the power dissipation efficiency increases with the increase in the strain in general. This is because the deformation time becomes longer with the strain increasing. Thus, the extent of the softening mechanisms, such as DRX and dynamic recovery (DRV), becomes higher. Thereby, the power dissipation efficiency increases. And the peak area of power dissipation efficiency (0.3) appears at the temperature of 500 °C with the strain rates of 0.01−1 s^{-1}. The high power dissipation efficiency zone of S50 is larger than that of S100, and the difference tends to decrease with the increasing strain. The high power dissipation efficiency zone is mainly concentrated in the high temperature range, indicating that the great

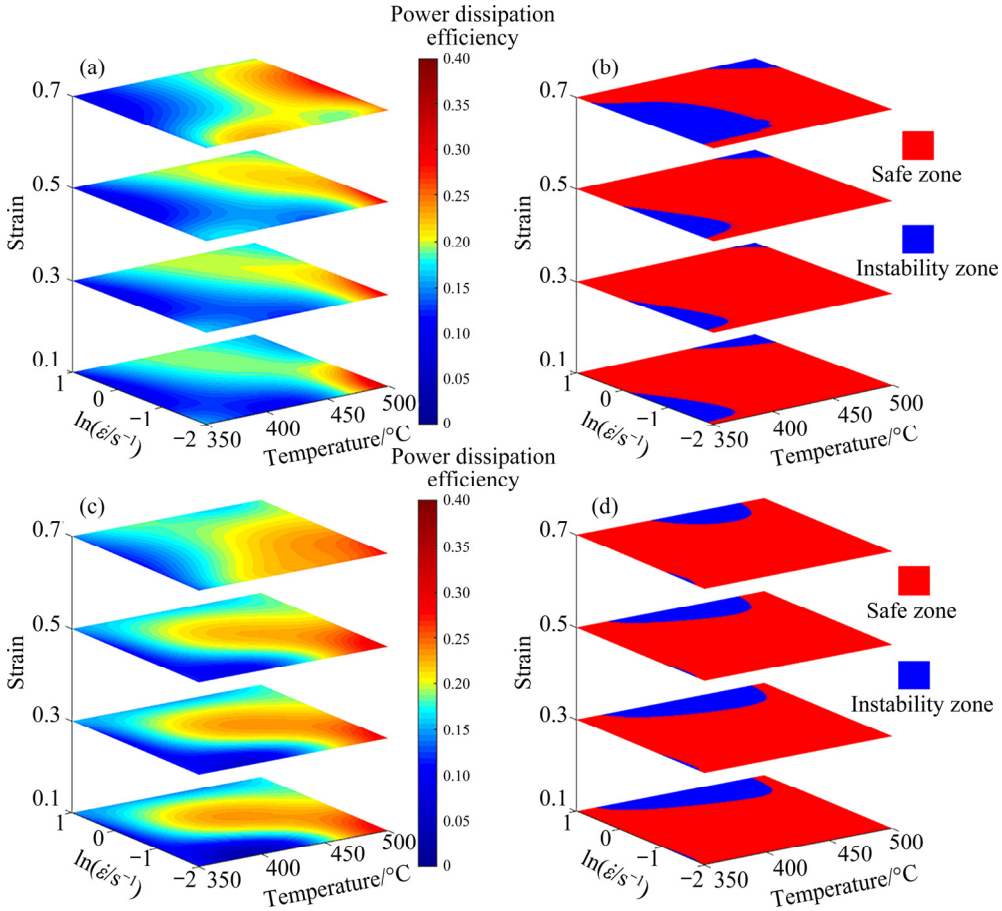

Fig. 5 3D power dissipation efficiency maps (a, c) and 3D instability maps (b, d) of different SC specimens: (a, b) S100; (c, d) S50

microstructure changes in the 6082 aluminum alloy. From Fig. 5(b) and Fig. 5(d), it can be seen that the high power dissipation efficiency zone is mainly distributed in the safe zone, except the zone at the upper-right corner in Fig. 5(b). Considering the instability zone under different strains during deformation, these zones should be superimposed in the hot processing map of the whole deformation process.

The hot processing maps of S100 and S50 in the whole deformation process are shown in Fig. 6, in which the contours represent the power dissipation efficiency, and the gray zones stand for the instability zone. The value of power dissipation efficiency increases with the increase of the temperature overall. In Fig. 6(a), the main instability zones of S100 locate at the temperatures of 350−420 °C with strain rates of 0.03−1 s^{-1} and at the temperatures of 440−500 °C with the strain rates of 1−10 s^{-1}, which should be avoided. High power dissipation efficiency areas of S100 locate in two main domains. Domain I is at the temperatures of 430−500 °C with the strain rates of 0.01−1 s^{-1}, in which DRX probably occurs. Domain II is at the temperatures of 370−430 °C with low strain rates of 0.01−0.015 s^{-1}, in which the range of strain rate is too narrow to control for processing. In Fig. 6(b), the main instability zone of S50 locates at the temperatures of 360−480 °C with the strain rates of 1−10 s^{-1} and there are three main high power dissipation efficiency domains for S50. Domain I is at the temperatures of 430−500 °C with the strain rates of 0.01−1 s^{-1}, Domain II is at the temperatures of 480−500 °C with the strain rates of 1−10 s^{-1}, and Domain III is at low temperatures of 410−430 °C with low strain rates of 0.01−0.1 s^{-1}, in which the optimum strain rate increases with the increase of temperature. In addition, the instability zones of S100 appear in the area of the low temperature and low strain, and in the area of high temperature and high strain rate, while that of S50 distributes in the area of high strain rate with the temperatures of 360−480 °C, indicating that the SC pressure has a great influence on the hot workability of 6082 aluminum alloy. Considering the fact that the pressures of different parts of a complex component are different during SC, the optimum parameters should be both suitable for S100 and S50. Thus, the optimum processing parameters are the temperatures of 430−500 °C and the strain rates of 0.01−1 s^{-1}.

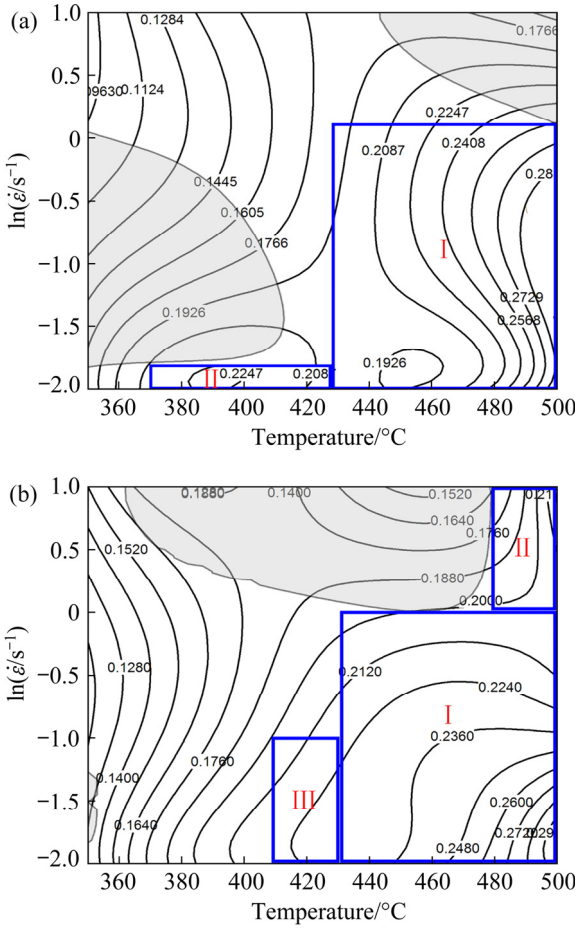

Fig. 6 Hot processing maps of different SC specimens: (a) S100; (b) S50

3.4 Microstructure evolution during hot compression

3.4.1 Influence of temperature

To elaborate on the relationship among microstructure evolution, SC pressure, and deformation conditions, the microstructures of specimens with different power dissipation efficiencies and thermal conditions were analyzed through EBSD. Figure 7 presents the EBSD results of S100 deformed at the strain rate of 0.01 s^{-1} and the temperatures of 350, 400, 450, and 500 °C. Table 2 shows the corresponding statistical results of Fig. 7. Black and red lines represent high-angle grain boundaries (HAGBs, misorientation angle higher than 15°) and low-angle grain boundaries (LAGBs, misorientation angle lower than 15° and higher than 2°), respectively. The calculation method of DRX volume fraction is based on grain orientation spread (GOS) value from EBSD results and illustrated in detail in Ref. [32]. From Fig. 7(a), the microstructure is mainly composed of large-

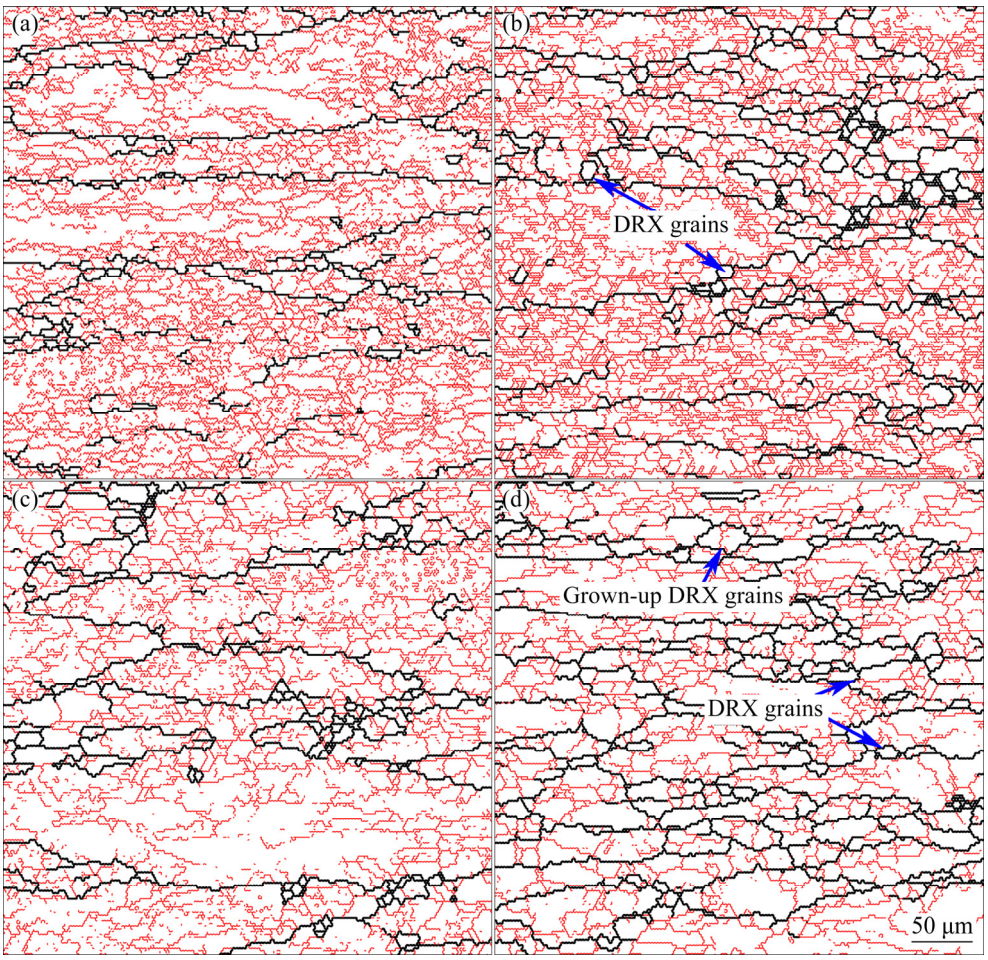

Fig. 7 EBSD results of S100 deformed at $\dot{\varepsilon}$=0.01 s^{-1} and different temperatures with strain of 0.69: (a) T=350 °C; (b) T=400 °C; (c) T=450 °C; (d) T=500 °C (Black and red lines represent HAGBs and LAGBs, respectively)

Table 2 Statistical results of S100 deformed at strain rate of 0.01 s^{-1} and different temperatures with strain of 0.69

Deformation temperature/°C	LAGB fraction/%	DRX volume fraction/%
350	84.1	1.0
400	77.3	2.8
450	75.9	5.7
500	57.5	13.3

sized elongated grains at a low temperature (350 °C). The LAGBs fraction is 84.1% and the DRX volume fraction is 1.0%, indicating that DRV is the dominant softening mechanism. Thus, the corresponding power dissipation efficiency (0.15) is the lowest. As the deformation temperature reaches 400 °C in Fig. 7(b), the grain boundaries become serrated and the fraction of LAGBs is reduced to 77.3%, and small-sized grains with hardly any inner substructure appear at grain boundaries. This indicates that DRX occurs in this condition. With the temperature increasing, the LAGBs fraction is reduced to 75.9% at 450 °C (Fig. 7(c)) and reaches the lowest value of 57.5% at 500 °C (Fig. 7(d)). The DRX volume fraction in Fig. 7(d) reaches the highest value of 13.3%, which has the highest power dissipation efficiency (0.28) in Fig. 7. Besides, several DRX grains have grown up and more grains change from the elongated shape into isometric shape at relatively high temperature. Generally, in the hot compression process of 6082 aluminum alloy, the atomic motion and dislocation motion become more active with the temperature increasing, resulting in more dislocations absorbed by LAGBs. Therefore, more LAGBs evolve into HAGBs, the fraction of LAGBs decreases, and the DRX volume fraction increases. Thus, power dissipation efficiency increases gradually with the increase of the temperature, except that the power dissipation efficiency in Fig. 7(b) (0.225) is slightly higher than that in Fig. 7(c) (0.19). The microstructure in Fig. 7(b)

has more substructure inside the grains and less DRX volume fraction than that in Fig. 7(c), indicating that DRV and DRX coexist but the extent is different in these two thermal conditions [33], and thus the transition of the major energy consumption from DRV to DRX could be the reason for the fluctuation in power dissipation efficiency. It can be seen from the EBSD results that the DRX volume fraction is relatively low. DRV is prone to occur for the high stacking fault energy of aluminum alloy, thus DRX is prohibited. Therefore, a higher proportion of DRX is beneficial to obtaining fine microstructure in aluminum alloy, but DRV is still a very important deformation mechanism.

3.4.2 Influence of deformation degree

Figure 8 shows the EBSD results of S100 deformed at different strains under the strain rate of 0.01 s^{-1} and the temperature of 400 °C, and the corresponding statistical results are shown in Table 3 (The statistical results at strain of 0.69 are also listed in Table 3). From Fig. 8(a), it can be observed that grains are compressed in the deformation direction with the strain of 0.30, and the LAGB fraction is relatively high and unevenly distributed among different grains. DRX can hardly be observed (DRX volume fraction is 0.1%). This indicates that the strain is concentrated in some grains in the initial stage of deformation, and dislocations generated in deformation are rearranged into substructures through DRV. From Fig. 8(b), it can be observed that the fraction of LAGBs increases obviously with the strain increasing to 0.50, while the change of LAGB fraction is small. Discontinuous HAGBs generated from grain fragmentation can be observed and the DRX volume fraction (0.6%) remains low, which means that higher strain energy is stored and DRV is still the dominant soften mechanism. The LAGB fraction decreases with the strain increasing to 0.69 and DRX can be observed (DRX volume is 2.8%). DRX consumes the dislocations and strain energy is accumulated during deformation and becomes the dominant soften mechanism. The microstructure evolution explains the change of the hot processing map with the strain, while the flow stress only decreases slightly with the strain increasing.

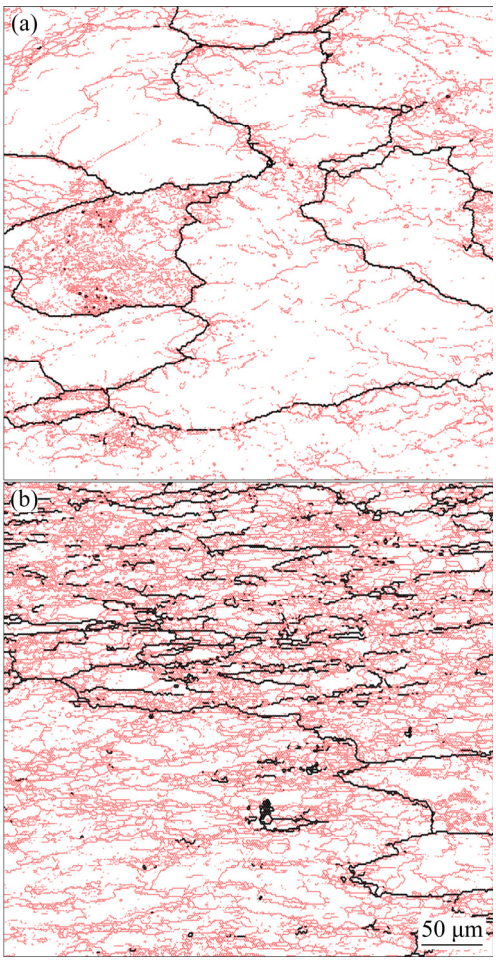

Fig. 8 EBSD results of S100 deformed at 400 °C, $\dot{\varepsilon}$=0.01 s^{-1} and different strains: (a) ε=0.30; (b) ε=0.50

Table 3 Statistical results of S100 deformed at T=400 °C, $\dot{\varepsilon}$=0.01 s^{-1} and different strains

Deformation strain	LAGB fraction/%	DRX volume fraction/%
0.30	85.3	0.1
0.50	83.8	0.6
0.69	77.3	2.8

3.4.3 Microstructure in different zones of hot process map

Figure 9 shows the EBSD results of S100 deformed under different thermal conditions. And the corresponding LAGBs fraction and DRX volume fraction are shown in Table 4. By comparing Fig. 7(b) with Fig. 9(a), and Fig. 7(c) with Fig. 9(b), it can be observed that the size of DRX grains decreases with the increase of the strain rate at the same temperature. A low strain rate provides adequate time for DRX, which means that more LAGBs grow into HAGBs by absorbing dislocations. As can be seen in Table 2 and Table 4, the fraction of LAGBs decreases with the increase of the strain rate. Thereby, the power dissipation efficiency in Fig. 7(b) (0.225) is higher than Fig. 9(a) (0.176). Besides, Fig. 9(a) is in the

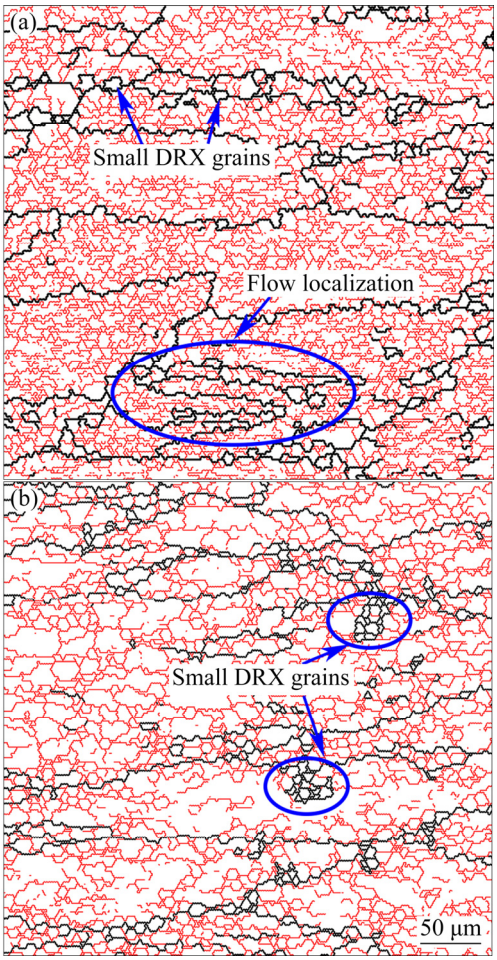

Fig. 9 EBSD results of S100 deformed under different thermal conditions with strain of 0.69: (a) T=400 °C, $\dot{\varepsilon}$=0.1 s^{-1}; (b) T=450 °C, $\dot{\varepsilon}$=1 s^{-1}

Table 4 Statistical results of S100 deformed under different thermal conditions with strain of 0.69

Deformation condition	LAGB fraction/%	DRX volume fraction/%
T=400 °C, $\dot{\varepsilon}$=0.1 s^{-1}	79.8	2.9
T=450 °C, $\dot{\varepsilon}$=1 s^{-1}	75.6	6.9

instability zone. A narrow band-like structure marked as flow localization can be observed in Fig. 9(a). The strain rate is higher and the temperature is lower under this condition, which means the hot deformation would be completed in a short time. Thus, the deformation heating effect becomes significant and a large amount of plastic work cannot be released into the surrounding material effectively. Both factors lead to temperature increasing locally, and the local softening effect becomes higher and results in flow localization [34]. The flow localization instability characteristics suggest that parameters in this domain should be avoided in deformation.

Figure 10 shows the EBSD results of S100 deformed in high power dissipation efficiency zone at different temperatures, and the corresponding fractions of LAGBs and DRX are shown in Table 5. The power dissipation efficiency increases from 0.208 to 0.280 with the temperature increasing from 450 to 500 °C at the strain rate of 0.1 s^{-1}. It can be seen that small DRX grains are distributed at the edge of grain boundaries in Fig. 10(a). It can be seen that the LAGBs fraction in Fig. 10(a) (74.1%) is slightly higher than that in Fig. 10(b) (71.6%)

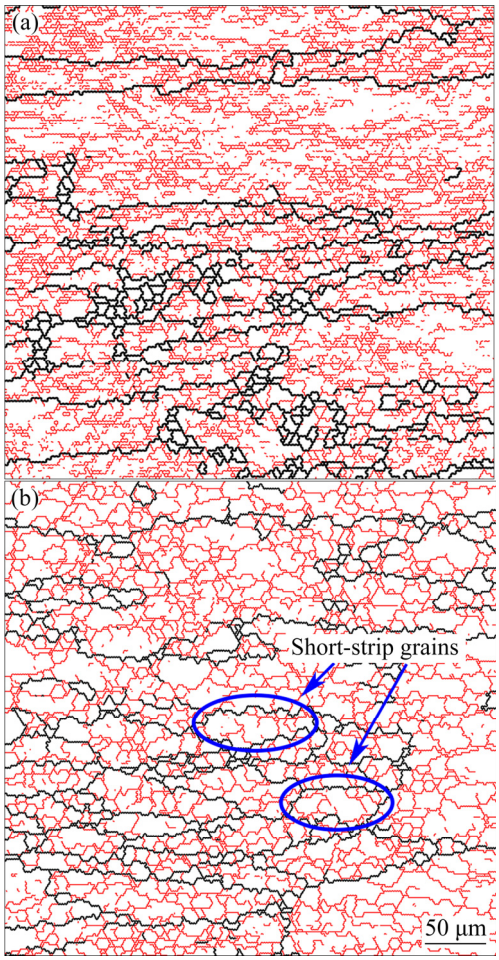

Fig. 10 EBSD results of S100 deformed in high power dissipation efficiency zone with strain of 0.69: (a) T=450 °C, $\dot{\varepsilon}$=0.1 s^{-1}; (b) T=500 °C, $\dot{\varepsilon}$=0.1 s^{-1}

Table 5 Statistical results of S100 deformed in high dissipation rate zone with strain of 0.69

Deformation condition	LAGB fraction/%	DRX volume fraction/%
T=450 °C, $\dot{\varepsilon}$= 0.1 s^{-1}	74.1	6.1
T=500 °C, $\dot{\varepsilon}$=0.1 s^{-1}	71.6	8.2

while the DRX volume fraction in Fig. 10(a) (6.1%) is lower than that in Fig. 10(b) (8.2%). As shown in Fig. 10(b), the long-strip grains decrease and the short-strip grains increase at higher temperatures and the DRX grain size is larger, indicating that the lower strain rate can provide more time for the DRX grain growth. The power dissipation efficiency in Fig. 10(b) is higher.

3.4.4 Influence of SC pressure

Figure 11 shows the EBSD results of S50 deformed under different thermal conditions and Table 6 shows the corresponding fractions of LAGBs and DRX volume. Large-sized DRX grains can be observed in Fig. 11(a) (T=400 °C, $\dot{\varepsilon}$ = 0.01 s^{-1}) and the LAGBs fraction is 80.2%. Additionally, the DRX grains of S100 deformed under the same deformation condition (Fig. 7(b)) are much finer, and the DRX volume fraction of S100 (2.8%) is lower than that of S50 (14.0%). As mentioned above, the initial microstructure of S100 contains finer grains and more second phase particles than that of S50. Fine-grain structure is beneficial to the nucleation of DRX [35,36]. And due to the weak pinning effect of second phase particles in S50, newly formed fine DRX grains are more prone to grow up at a longer deformation time. Thus, Fig. 11(a) possesses more grown-up DRX grains and a higher DRX volume fraction while Fig. 7(b) contains more fine DRX grains. This result implies that the initial SC pressure has a great influence on the microstructure evolution during hot compression. But the grain size of DRX in Fig. 11(b) and Fig. 11(c) is similar to that in Fig. 7(c) and Fig. 10(a), respectively, and the relative statistical data in Table 6 become closer compared with Fig. 11(a) and Fig. 7(b). The difference between DRX nucleation of fine and coarse microstructures decreases at higher deformation temperatures. Meanwhile, the second phase particles are dissolved to a great extent and the pinning effect is greatly weakened in both S100 and S50. The conclusion can be drawn that high temperature decreases the influence of the initial microstructure of S50 and S100.

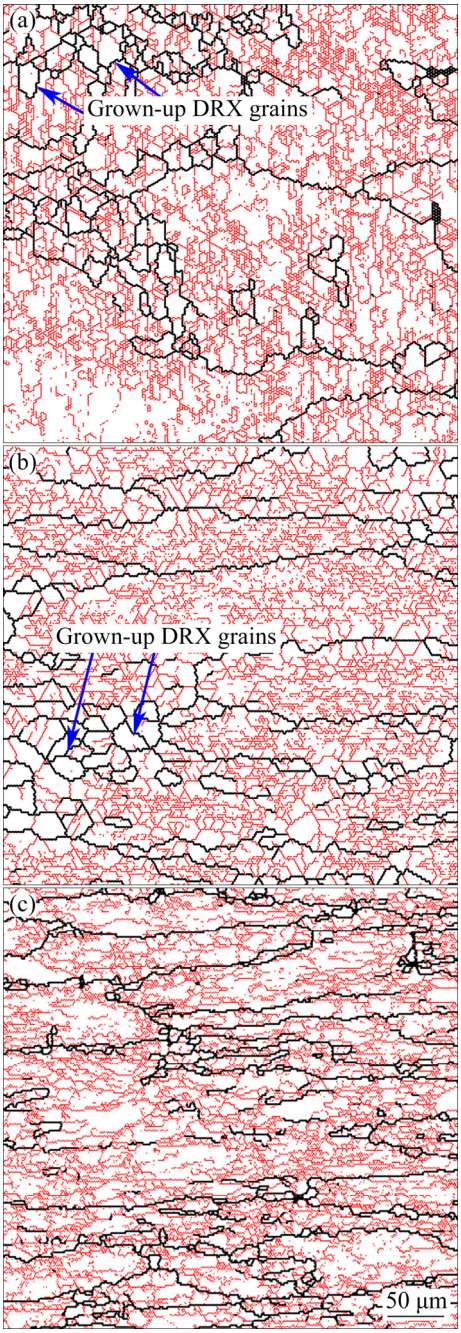

Fig. 11 EBSD results of S50 deformed under different thermal conditions with strain of 0.69: (a) T=400 °C, $\dot{\varepsilon}$=0.01 s^{-1}; (b) T=450 °C, $\dot{\varepsilon}$=0.01 s^{-1}; (c) T=450 °C, $\dot{\varepsilon}$=0.1 s^{-1}

Table 6 Statistical results of S50 and S100 deformed under different thermal conditions with strain of 0.69

Deformation condition	LAGB fraction/%	DRX volume fraction/%
T=400 °C, $\dot{\varepsilon}$ = 0.01 s^{-1}, S50	80.2	14.0
T=400 °C, $\dot{\varepsilon}$ = 0.01 s^{-1}, S100	77.3	2.8
T=450 °C, $\dot{\varepsilon}$ = 0.01 s^{-1}, S50	79.8	10.7
T=450 °C, $\dot{\varepsilon}$ = 0.01 s^{-1}, S100	75.9	5.7
T = 450 °C, $\dot{\varepsilon}$ =0.1 s^{-1}, S50	75.0	9.1
T = 450 °C, $\dot{\varepsilon}$ =0.1 s^{-1}, S100	74.1	6.1

Figure 12 shows the EBSD results of S50 deformed at the strain rate of 0.1 s^{-1} and the temperature of 400 °C. Grown-up DRX grains can

be observed in Fig. 12, which is consistent with the results above. The grain size of DRX in Fig. 12 is smaller than that in Fig. 11(a) because of the higher strain rate. Compared with Fig. 9(a), no obvious flow localization is observed in Fig. 12, indicating that SC pressure is closely related to the generation of the instability zone. Figure 13 shows the second phase distribution of S50 and S100 deformed at a temperature of 400 °C and a strain rate of 0.1 s^{-1}. It can be seen that the particles in the two samples are dissolved to different degrees, the second phase particles in Fig. 13(a) are concentrated in several areas of the matrix, while in Fig. 13(b) the second phase particles are evenly distributed in the aluminum matrix. The specimens with non-uniform second phase distribution have uneven stress distribution during deformation, which leads to the local softening and the uneven deformation. Thus, flow localization is likely to occur.

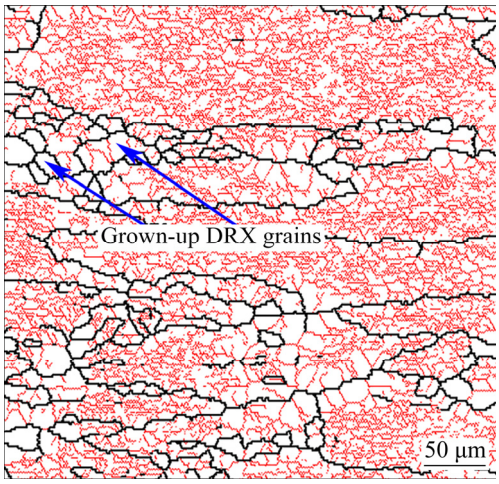

Fig. 12 EBSD result of S50 deformed at strain rate of 0.1 s^{-1} and temperature of 400 °C with strain of 0.69

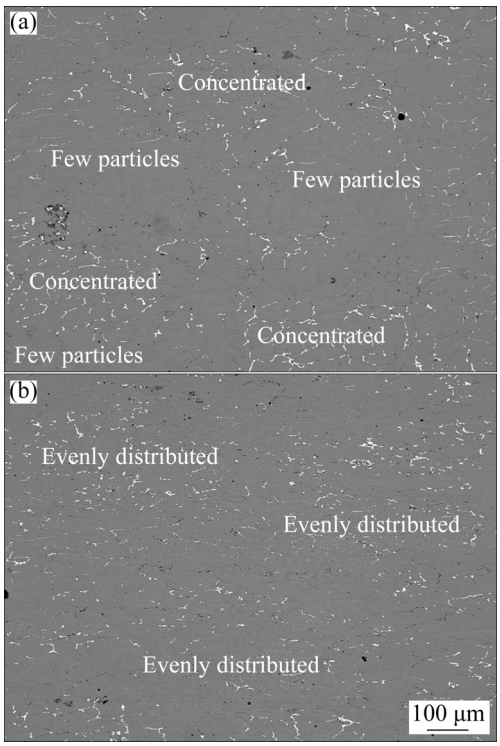

Fig. 13 EPMA results showing second phase distribution of specimens deformed at strain rate of 0.1 s^{-1} and temperature of 400 °C with strain of 0.69: (a) S100; (b) S50

Considering that SC pressures applied at different parts of complex components during the squeeze casting process are different, the optimum process parameters are temperatures of 430−500 °C and strain rates of 0.01−1 s^{-1}. In this range, the power dissipation efficiency of deformation is high and the microstructure is ideal.

4 Conclusions

(1) The 6082 aluminum alloy fabricated under higher SC pressure exhibits higher flow stress because of the finer grains, higher density of second phase particles, and more dispersoids. The gap in the flow stress of the aluminum alloy under different SC pressures decreases with the increase of the deformation temperature.

(2) The hot processing maps can be used to well predict the processing properties of SC 6082 aluminum alloy. The optimum processing parameters are proposed at the temperatures of 430−500 °C and the strain rates of 0.01−1 s^{-1}. Specimens deformed under optimum processing conditions have good hot workability and satisfactory microstructure.

(3) DRX is more likely to occur on the compressed specimens fabricated under higher SC pressure and the size of DRX grains is smaller. High temperature can weaken the difference of the hot deformation behavior between different SC samples because the pinning effect of the second phase particle is greatly reduced.

(4) Uneven second phase particles in the S100 result in flow localization instability during compression at low temperatures and middle strain rates.

Acknowledgments

This study was financially supported by the National Natural Science Foundation of China

(Nos. 52090043, 51725504), the Key Research and Development Program of Hubei Province, China (No. 2020BAB040), and the Fundamental Research Funds for the Central Universities, China (No. 2021GCRC003). The authors are also grateful for the technical assistance from the Analytical Platform of the State Key Laboratory of Materials Processing and Die & Mould Technology and the Analytical and Testing Center of Huazhong University of Science and Technology, China.

References

[1] QIAN X M, PARSON N, CHEN X G. Effects of Mn addition and related Mn-containing dispersoids on the hot deformation behavior of 6082 aluminum alloys [J]. Materials Science and Engineering A, 2019, 764: 138253.

[2] FAN R J, ATTARILAR S, SHAMSBORHAN M, EBRAHIMI M, GÖDE C, ÖZKAVAK H V. Enhancing mechanical properties and corrosion performance of AA6063 aluminum alloys through constrained groove pressing technique [J]. Transactions of Nonferrous Metals Society of China, 2020, 30: 1790−1802.

[3] CHANG Y L, HUNG F Y, LUI T S. Study of microstructure and tensile properties of infrared-heat-treated cast-forged 6082 aluminum alloy [J]. Journal of Materials Research and Technology, 2019, 8: 173−179.

[4] BIROL Y, ILGAZ O, AKDI S, UNUVAR E. Comparison of cast and extruded stock for the forging of AA6082 alloy suspension parts [J]. Advanced Materials Research, 2014, 939: 299−304.

[5] BIROL Y, ILGAZ O. Effect of cast and extruded stock on grain structure of EN AW 6082 alloy forgings [J]. Materials Science and Technology, 2014, 30: 860−866.

[6] THAM L M, GUPTA M, CHENG L. Influence of processing parameters on the near-net shape synthesis of aluminium-based metal matrix composites [J]. Journal of Materials Processing Technology, 1999, 89/90: 128−134.

[7] DEDOV S, LEHMANN G, KAWALLA R. Application of combined casting-forging process for production of durable lightweight aluminum parts [J]. Key Engineering Materials, 2013, 554/555/556/557: 264−273.

[8] CHEN H Q, WANG Q C, GUO H G. Research on the casting-forging precision forming process of alternator poles [J]. Journal of Materials Processing Technology, 2002, 129: 330−332.

[9] BIROL Y, AKDI S. Cooling slope casting to produce EN AW 6082 forging stock for manufacture of suspension components [J]. Transactions of Nonferrous Metals Society of China, 2014, 24: 1674−1682.

[10] GUO S J, XU Y, HAN Y, LIU J Y, XUE G X, NAGAUMI H. Near net shape casting process for producing high strength 6xxx aluminum alloy automobile suspension parts [J]. Transactions of Nonferrous Metals Society of China, 2014, 24: 2393−2400.

[11] LI D M, GHOSH A. Tensile deformation behavior of aluminum alloys at warm forming temperatures [J]. Materials Science and Engineering A, 2003, 352: 279−286.

[12] RODRIGUES A V, LIMA T S, VIDA T A, BRITO C, GARCIA A, CHEUNG N. Microstructure features and mechanical/electrochemical behavior of directionally solidified Al−6wt.%Cu−5wt.%Ni alloy [J]. Transactions of Nonferrous Metals Society of China, 2021, 31: 1529−1549.

[13] SCHINDLER I, KAWULOK P, OČENÁŠEK V, OPĚLA P, KAWULOK R, RUSZ S. Flow stress and hot deformation activation energy of 6082 aluminium alloy influenced by initial structural state [J]. Metals, 2019, 9: 1248.

[14] MORAKABATI M, HAJARI A. Hot working behavior of near alpha titanium alloy analyzed by mechanical testing and processing map [J]. Transactions of Nonferrous Metals Society of China, 2020, 30: 1560−1573.

[15] LIAO H C, WU Y, ZHOU K X, YANG J. Hot deformation behavior and processing map of Al–Si–Mg alloys containing different amount of silicon based on Gleebe−3500 hot compression simulation [J]. Materials & Design, 2015, 65: 1091−1099.

[16] CAI Z W, CHEN F X, MA F J, GUO J Q. Dynamic recrystallization behavior and hot workability of AZ41M magnesium alloy during hot deformation [J]. Journal of Alloys and Compounds, 2016, 670: 55−63.

[17] WANG S, HOU L G, LUO J R, ZHANG J S, ZHUANG L Z. Characterization of hot workability in AA 7050 aluminum alloy using activation energy and 3-D processing map [J]. Journal of Materials Processing Technology, 2015, 225: 110−121.

[18] SUN Y, CAO Z H, WAN Z P, HU L X, YE W H, LI N K, FAN C L. 3D processing map and hot deformation behavior of 6A02 aluminum alloy [J]. Journal of Alloys and Compounds, 2018, 742: 356−368.

[19] GHOMASHCHI M R, VIKHROV A. Squeeze casting: An overview [J]. Journal of Materials Processing Technology, 2000, 101: 1−9.

[20] FAN C H, CHEN Z H, HE W Q, CHEN J H, CHEN D. Effects of the casting temperature on microstructure and mechanical properties of the squeeze-cast Al−Zn−Mg−Cu alloy [J]. Journal of Alloys and Compounds, 2010, 504: L42−L45.

[21] MRÓWKA-NOWOTNIK G, SIENIAWSKI J. Influence of heat treatment on the microstructure and mechanical properties of 6005 and 6082 aluminium alloys [J]. Journal of Materials Processing Technology, 2005, 162/163: 367−372.

[22] GUO L G, YANG S, YANG H, ZHANG J. Processing map of as-cast 7075 aluminum alloy for hot working [J]. Chinese Journal of Aeronautics, 2015, 28: 1774−1783.

[23] PARVIZIAN F, GÜZEL A, JÄGER A, LAMBERS H G, SVENDSEN B, TEKKAYA A E, MAIER H J. Modeling of dynamic microstructure evolution of EN AW-6082 alloy during hot forward extrusion [J]. Computational Materials Science, 2011, 50: 1520−1525.

[24] DAI Q S, DENG Y L, TANG J G, WANG Y. Deformation characteristics and strain-compensated constitutive equation for AA5083 aluminum alloy under hot compression [J]. Transactions of Nonferrous Metals Society of China, 2019, 29: 2252−2261.

[25] CHEN G, LIN F Y, YAO S J, HAN F, WEI B, ZHANG Y M. Constitutive behavior of aluminum alloy in a wide

temperature range from warm to semi-solid regions [J]. Journal of Alloys and Compounds, 2016, 674: 26−36.
[26] XU Z L, MA H J, ZHAO N, HU Z L. Investigation on compressive formability and microstructure evolution of 6082-T6 aluminum alloy [J]. Metals, 2020, 10: 469.
[27] LIN J G. Fundamentals of materials modelling for metals processing technologies: Theories and applications [M]. Singapore: World Scientific Publishing Company, 2015: 30−91.
[28] RAJAMUTHAMILSELVAN M, RAMANATHAN S, KARTHIKEYAN R. Processing map for hot working of SiC_p/7075 Al composites [J]. Transactions of Nonferrous Metals Society of China, 2010, 20: 668−674.
[29] WANG Y X, ZHAO G Q, XU X, CHEN X X, ZHANG C S. Constitutive modeling, processing map establishment and microstructure analysis of spray deposited Al−Cu−Li alloy 2195 [J]. Journal of Alloys and Compounds, 2019, 779: 735−751.
[30] CHEN X R, LIAO Q Y, NIU Y X, JIA Y H, LE Q C, NING S C, HU C L, HU K, YU F X. Comparison study of hot deformation behavior and processing map of AZ80 magnesium alloy casted with and without ultrasonic vibration [J]. Journal of Alloys and Compounds, 2019, 803: 585−596.
[31] SON K T, KIM M H, KIM S W, LEE J W, HYUN S K. Evaluation of hot deformation characteristics in modified AA5052 using processing map and activation energy map under deformation heating [J]. Journal of Alloys and Compounds, 2018, 740: 96−108.
[32] WANG X Y, WANG D K, JIN J S, LI J J. Effects of strain rates and twins evolution on dynamic recrystallization mechanisms of austenite stainless steel [J]. Materials Science and Engineering A, 2019, 761: 138044.
[33] LI C, LIU K, CHEN X G. Improvement of elevated-temperature strength and recrystallization resistance via Mn-containing dispersoid strengthening in Al−Mg−Si 6082 alloys [J]. Journal of Materials Science & Technology, 2020, 39: 135−143.
[34] ZHANG J Q, DI H S. Deformation heating and flow localization in Ti−15−3 metastable β titanium alloy subjected to high Z deformation [J]. Materials Science and Engineering A, 2016, 676: 506−509.
[35] SINGH D, JAYAGANTHAN R, RAO P N, KUMAR A, VENKETESWARLU D. Effect of initial grain size on microstructure and mechanical behavior of cryorolled AA 5083 [J]. Materials Today: Proceedings, 2017, 4: 7609−7617.
[36] ZHANG J X, MA M, LIU W C. Effect of initial grain size on the recrystallization and recrystallization texture of cold-rolled AA 5182 aluminum alloy [J]. Materials Science and Engineering A, 2017, 690: 233−243.

挤压铸造态 6082 铝合金的加工图及热变形行为

邓 磊[1]，张海栋[1]，李国爱[2]，唐学峰[1]，易蒲淞[1]，刘 钊[1]，王新云[1]，金俊松[1]

1. 华中科技大学 材料成形与模具技术国家重点实验室，武汉 430074；
2. 中国航发北京航空材料研究院，北京 100095

摘 要：研究在不同压力下由挤压铸造工艺制备的 6082 铝合金的热变形行为和显微组织演化。对合金进行热压缩实验并建立 3D 热加工图。采用光学显微镜、扫描电子显微镜以及背散射电子衍射技术研究合金的显微组织演化。结果表明，在较高挤压铸造压力下得到的试样在热变形过程中产生较多动态再结晶晶粒。在高温下由于第二相颗粒的溶解，挤压铸造压力对热变形后显微组织的影响减弱。此外，当较高挤压铸造压力下制备的样品在低温及中等应变速率下变形时，不均匀第二相分布容易导致流变失稳的发生。最后，得到挤压铸造态 6082 铝合金的最优加工区域为 430~500 ℃和 0.01~1 s^{-1}。

关键词：6082 铝合金；挤压铸造；变形行为；加工图；动态再结晶

(Edited by Wei-ping CHEN)